Research Article Vol. 34, No. 19 / 21 Sep 2026 / Optics Express 36278
Optics EXPRESS

Electrically-driven monolithic silicon photonic isolator based on seedlayer-free bismuth terbium iron garnet

LUIGI RANNO,[1,†] YIHONG SUN,[2,†] KENSUKE HAYASHI,[1,3] LOUIS MARTIN-MONIER,[1] PETE EISMONT LAUER,[1] SHUOQIU TIAN,[2] VINH HUY NGUYEN TO,[2] SAMUEL SERNA,[1] ZHIYUN XU,[1] TUSHAR SANJAY KARNIK,[1] COSMIN CONSTANTIN POPESCU,[1] XUJIE TONG,[2] HONG WANG,[2] CAROLINE A. ROSS,[1] JUEJUN HU,[1] AND JIA XU BRIAN SIA[2,*]

[1]*Department of Materials Science & Engineering, Massachusetts Institute of Technology, Cambridge, M.A., USA*
[2]*School of Electrical and Electronic Engineering, Nanyang Technological University, 50 Nanyang Avenue, 639798, Singapore*
[3]*Department of Materials Physics, Nagoya University, Furo-cho, Chikusa-ku, Nagoya, 464-8603, Japan*
[†]These authors contributed equally to this work.
[*]*jiaxubrian.sia@ntu.edu.sg*

Abstract: Photonic isolation is an essential on-chip function needed to stabilize laser operation and prevent cross-talk between different components within a communication system. Monolithically integrated isolator designs incorporate magneto-optical cladding consisting of doped yttrium iron garnet (YIG), such as cerium-doped YIG (Ce:YIG) and bismuth-doped YIG (Bi:YIG), where a YIG seedlayer is required prior to the deposition and subsequent crystallization of doped YIG. This adversely impacts isolator performance through reduced mode overlap with the doped YIG layer. Furthermore, the Faraday rotations of YIG and Ce:YIG have opposing signs such that they partially cancel out. This work demonstrates a seedlayer-free, monolithic nonreciprocal photonic platform based on an alternative garnet formulation, bismuth-doped terbium iron garnet (Bi:TbIG). We further realize on-chip integration of electromagnets to obviate the requirements of external magnets. An isolator based on the asymmetric Mach-Zehnder interferometer (MZI) architecture is implemented, which records a π nonreciprocal phase shift with a power consumption of 52 mW. Optical isolation as high as 24 dB is achieved.

© 2026 Optica Publishing Group under the terms of the Optica Open Access Publishing Agreement

1. Introduction

Driven by advanced silicon manufacturing [1–4], silicon photonics have proved to be a disruptive technology platform [5–7]. This is in spite of the inherent material limitations (e.g., indirect bandgap and lack of magneto-optical non-reciprocity or Pockels effect) pertaining to silicon. Moving on from optical communications, silicon photonics has diversified towards various distinct applications (e.g., neuromorphic computing [5], quantum photonics [6] and sensing [7]), necessitating an increase in the complexity of photonic integrated circuits (PICs). As PICs increase in sophistication, optical isolation is imperative for several reasons. 1) Isolators will take on an increasingly critical role in minimizing backward reflections in complex PICs, which may bring about unwanted crosstalk and system instabilities. For instance, in optical communications, delayed back reflections arrive at different times. This results in the spreading of pulses and thereby, the reduction of the maximum attainable bit rate-distance product due to multi-path dispersion [8]. 2) Parasitic reflections feeding back into the laser typically result in an increase in laser instabilities and noise (i.e., relative intensity and frequency noises) [9]. More severe

#605422 https://doi.org/10.1364/OE.605422
Journal © 2026 Received 14 May 2026; revised 26 Jul 2026; accepted 2 Sep 2026; published 16 Sep 2026

Optics EXPRESS

consequences involve irreversible damage to the laser sources [10]. 3) Residual reflections from high-index contrast silicon waveguides can trigger parasitic lasing in on-chip amplifiers [11].

To that effect, there has been significant work in the development of optical isolators, in which the enabling mechanisms can be categorized into several categories: spatiotemporal modulation [12,13], nonlinearity (i.e., Kerr, cross-phase modulation [14], four-wave mixing [15], Brillouin scattering [16], Pockels effect [17]), and magneto-optical (MO) effect [18–28]. It is of note that conventional nonlinear isolators are fundamentally constrained by dynamic reciprocity, which limits their operation to pulsed signals [29]. Recent theoretical studies have shown that non-Hermitian photonic systems exploiting saturable absorption may circumvent this limitation, with numerical simulations predicting broadband nonreciprocal transmission under continuous-wave excitation [30,31]. On the other hand, while spatiotemporal modulation enables isolation with insertion loss as low as 0.1 dB, these devices necessitate large power consumption (on the order of 100 mW and above) with narrow operation bandwidth [12,32]. MO isolators are advantageous in terms of bandwidth and power consumption, while being commensurate with continuous wave operation.

MO isolators can be realized via heterogeneous [18–21] or monolithic integration [23,33,34]. The former brings the MO layer (a die) in close proximity to the silicon photonic waveguide via direct or adhesive bonding [21]. In comparison to heterogeneous integration, monolithic deposition [33,34] is advantageous in terms of lower processing complexity, where requirements on sample cleanliness and planarity prior to bonding are alleviated. Furthermore, in heterogeneous integration, the large size of the bonded garnet die (e.g., $500 \times 500\,\mu m^2$) would imply that the photonic performance of other nearby components will be impacted, thereby limiting the integration density. For monolithic integration, the primary material-of-choice is cerium-substituted yttrium iron garnet (Ce:YIG) due to its low loss and high Faraday rotation (i.e., $-4800°/cm$ at 1550 nm) [18]. However, for Ce:YIG, it is challenging to promote the growth of the garnet phase over competing phases (i.e., CeO_2) on non-garnet substrates. Typically, this has necessitated the deposition of a YIG seed layer and annealing at elevated temperatures of up to 850 °C [33]. Alternative approaches have also been demonstrated where crystallization can be accomplished using a seedlayer above the MO layer [35], but for Bi:YIG/YIG the figure of merit is less favorable than for the seed layer underneath [28]. In spite of the significant Faraday rotation conferred by Ce:YIG, the need for the YIG seed layer introduces some limitations. Firstly, the YIG layer impacts isolator performance through a reduced mode overlap with the Ce:YIG layer. Furthermore, the Faraday rotations of YIG and Ce:YIG have opposite signs, which will serve to limit the nonreciprocal phase shift (NRPS) experienced by the waveguide.

For instance, a 45-nm-thick YIG layer was used to promote the crystallization of the Ce:YIG layer [36]. In such a scenario, as investigated by Dulal et al. [27], a Ce:YIG layer with a high Faraday rotation of $4500°/cm$ will only impart similar levels of NRPS as a seed-layer-free MO layer with Faraday rotation of $2000°/cm$ (both values at $\lambda = 1550\,nm$). This impacts isolator footprint and insertion loss. Therefore, the development of a seed-layer-free MO/silicon photonic platform is imperative.

2. Operating principle of the monolithic Bi:TbIG/silicon photonic isolator

This work presents the development [24,37] of a monolithic seedlayer-free Bi:TbIG/silicon photonic platform operating at the C-band Fig. 1(a). Bi:TbIG is chosen for its high FR combined with the ability to crystallize Tb garnets on Si without a seedlayer [22,25–28]. We demonstrate an optical isolator based on monolithic Bi:TbIG on silicon waveguides incorporating integrated electromagnets, enabling low driving current and power requirements. With monolithic integration, the thickness of the SiO_2 spacer (Fig. 1(b)) can be controlled to minimize operating current, while alleviating metal (Au electromagnet) optical absorption. Our process includes a significant reduction in the thermal budget required for monolithic garnet growth and crystallization (from

Optics EXPRESS

850 °C to 600 °C). This sets the stage for further reduction in annealing temperatures, potentially commensurating with the CMOS backend. Leveraging this platform, an asymmetric Mach Zehnder interferometer (MZI)-based photonic isolator operating at C-band is demonstrated. The isolation mechanism relies on the NRPS accumulated along the two MZI arms, rather than polarization rotation of the propagating light. It should be noted that the term "Faraday rotation" used in this paper refers to the material-level magneto-optical property that gives rise to NRPS. Experimental data indicate that a π phase shift between the counterpropagating lightwaves can be attained with driving currents as low as 114 mA, achieving isolation ratio up to 24 dB. The isolator operates in TM mode to ensure efficient adiabatic coupling to the magneto-optical layer. Although TE is the dominant mode in PICs, the TM operation of our device is readily accommodated by on-chip polarization rotators. Standard PDK components that add only $\lesssim$1 dB (0.3–0.5 dB each) without affecting the isolation ratio [38,39]. Direct TE-mode operation is also feasible on seedlayer-free garnet platforms [25]. For the present NRPS scheme, it would require garnet on the waveguide sidewalls to overlap the in-plane TE field. Achieving uniform sidewall deposition and crystallization remains an engineering challenge that is the subject of our ongoing work.

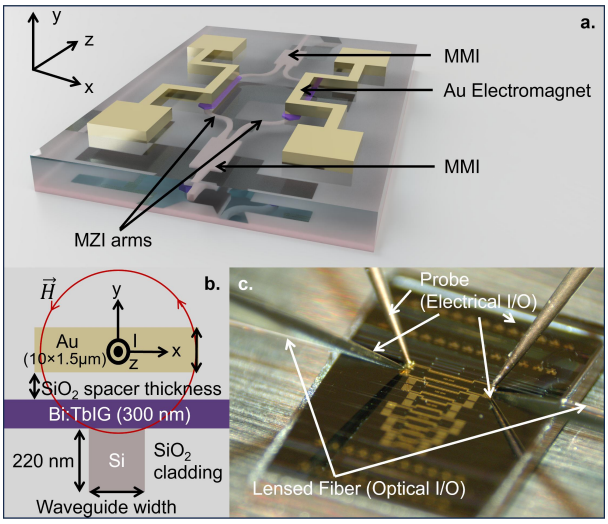


Fig. 1. (a) 3-D schematic of the electrically-driven MZI isolator based on the seedlayer-free monolithic Bi:TbIG/silicon nonreciprocal platform. The coordinate axes are defined with x in the transverse in-plane direction, y perpendicular to the chip surface, and z along the waveguide propagation direction. (b) Cross-sectional illustration (x-y plane) of the monolithically integrated Bi:TbIG/silicon waveguide. (c) Micrograph image of isolator with electrical probes (electrical I/O) and lensed fiber (optical I/O) annotated.

A 3-D schematic of the electrically-driven, monolithically integrated Bi:TbIG/Si MZI isolator is illustrated in Fig. 1(a). Figure 1(b) provides a cross-sectional illustration of the Bi:TbIG/Si waveguide and electromagnet. A micrograph image of the optical isolator chip is indicated in Fig. 1(c). The MZI is unbalanced, corresponding to an FSR of $\sim$ 8.5 nm. Identical lengths of integrated Bi:TbIG/Si waveguides with Au (1.5 μm-thick, and 10 μm-wide) driving electromagnets are implemented on both arms of the MZI. Through the application of currents on both electromagnets with equal amplitude and opposite directions, a static magnetic field perpendicular to the direction of current flow is generated, as defined by the Biot-Savart law. This results in the imaginary off-diagonal component ε_{xy} of the dielectric tensor (ε) of Bi:TbIG

Optics EXPRESS

to become non-zero due to the MO effect. NRPS of the waveguide is given by:

$$\Delta\beta_{\mathrm{TM}} = \frac{-4j\omega\varepsilon_0 \iint E_{\mathrm{op},y} \dfrac{\partial E_{\mathrm{op},y}}{\partial y}(KM_x)\, dA}{\beta_{\mathrm{TM}} \iint \left(\mathbf{E}_{\mathrm{op}} \times \mathbf{H}^*_{\mathrm{op}} + \mathbf{H}_{\mathrm{op}} \times \mathbf{E}^*_{\mathrm{op}}\right)_z dA} \tag{1}$$

where β_{TM}, ω, and ε_0 refer to the propagation constant of the TM mode, the angular frequency of light, and the vacuum permittivity, respectively. $\mathbf{E}_{\mathrm{op}}$ and $\mathbf{H}_{\mathrm{op}}$ denote the electric and magnetic fields of the guided optical mode, and $E_{\mathrm{op},y}$ is the y-component of $\mathbf{E}_{\mathrm{op}}$. The coefficient K captures the nonreciprocal Faraday ellipticity in its real part and the Faraday rotation in its imaginary part. M_x indicates the x-component of the Bi:TbIG magnetization (Fig. 1(b)). In our push-pull MZI configuration, a Bi:TbIG/Si waveguide length of $\pi/4 \times \Delta\beta_{\mathrm{TM}}$ is needed to realize complete optical isolation. Detailed derivations are shown in Supplement 1 S1. To induce a π phase shift between the forward and backward propagating lightwaves, the length of the nonreciprocal phase shifters are designated to be 1243 μm (Fig. 3(a)), corresponding to a NRPS of 632 rad/m (Fig. 3(c)).

3. Bi:TbIG silicon photonic platform

Detailed device fabrication process flow is elaborated in Supplement 1 S2. More specifically, 300 nm of Bi:TbIG ($Bi_{1.31}Tb_{1.88}Fe_5O_x$, Bi = 41%) is deposited into defined trenches on the MZI arms via pulsed-laser deposition (PLD) without a seedlayer (Fig. 1(b)). To avoid film cracking due to thermal expansion coefficient mismatch between Bi:TbIG and Si, an extended annealing process at lower temperature (600 °C, 10 hours) was utilized instead of rapid thermal annealing (850 °C, 5 minutes). Furthermore, slow thermal ramp up (10 °C per minute) and down (1 °C per minute) is adopted to avoid rapid thermal expansion. Because crystallization can be performed as a batch furnace step, many substrates can be annealed in parallel concurrently to the ongoing BEOL process where device throughput will not be limited by anneal duration. A possible future route toward a lower thermal budget is localized post-processing, such as integrated micro-heater [40] or laser annealing [41].

The optical constants of the Bi:TbIG garnet measured via ellipsometry are plotted in Supplement 1 S3. Ellipsometry measurements present more higher errors at low values of k (i.e., < 0.001), where the garnet might still contribute to significant waveguide propagation losses. To that effect, we characterize the propagation loss of the monolithic Bi:TbIG/Si waveguides via the cutback approach, where the propagation losses are found to be about 120 dB/cm. This value is dominated by absorption in the garnet, mainly attributed to Fe^{2+}/Fe^{4+} charge-transfer states linked to oxygen non-stoichiometry [28,42], with additional scattering from grain boundaries and patterned edges [43,44]. Being process-related rather than intrinsic, this loss can be reduced by optimizing the annealing ambient (O_2 partial pressure) and Bi content, consistent with the substantially lower losses of optimized garnet films on Si [28,37]. While the overall device insertion loss is approximately 12 dB, it is comparable to existing literature for integrated magneto-optical isolators [45–47]. Further loss reduction can be attained through optimization of the Bi substitution level and fabrication process, tapered garnet sections for effective mode transition, and optimal interaction length non-reciprocal phase shift of π. The phase purity of the deposited Bi:TbIG layer is investigated using X-ray diffraction (XRD) (Fig. 2), indicating polycrystalline garnet with no detectable secondary phases. A Bi:TbIG lattice constant of ~ 12.52 Å can be inferred from the XRD consistent with prior work [40].

Optics EXPRESS

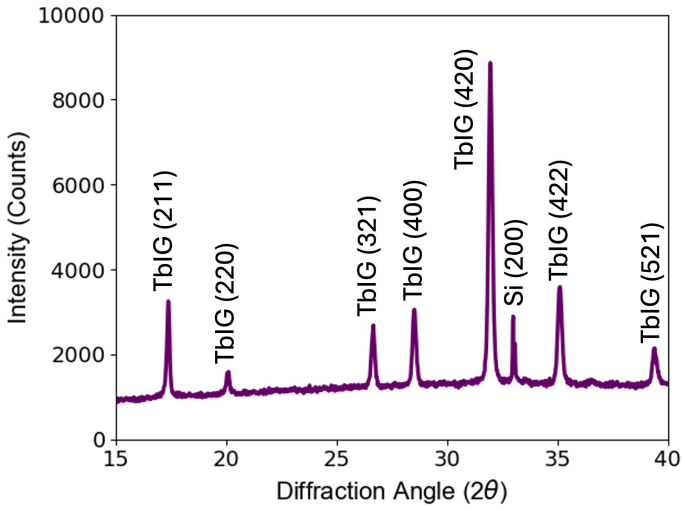


Fig. 2. XRD of the Bi:TbIG garnet on silicon where a single-phase polycrystalline garnet phase is validated.

4. Photonic isolator design

Following the development of the material platform, the Bi:TbIG (300 nm-thick)/Si (220 nm-thick) waveguide was designed for optimal NRPS. The Bi:TbIG layer is saturated at about 2000 Oe, with a Faraday rotation of $-1300°/\text{cm}$ at 1550 nm. Details of the Faraday rotation measurement for the Bi:TbIG layer, as well as the M-H loop of this formation can be found in our previous work [40]. At C-band, eigenmode calculations indicate single-mode operation for TM polarization at waveguide widths of less than 650 nm. Within the simulations, a driving current I_{driv} of 120 mA was implemented. Figure 3(a) plots the minimum Bi:TbIG/Si waveguide lengths (L_{min}) necessary to induce a π phase difference between the forward and backward propagating lightwave with varying waveguide width (400 – 650 nm) and SiO_2 spacer thickness (200 – 700 nm). For visual guidance, the corresponding waveguide widths and SiO_2 spacer thickness for L_{min} = 1220, 1230, 1240, 1250, and 1260 μm are annotated. Another important consideration with regards to the design of the Bi:TbIG/Si waveguide is the impact of the Au electromagnets absorption loss. In Fig. 3(b), the parameter space of Fig. 3(a) is replicated, where the contribution from metal absorption is simulated. The corresponding parameters for parasitic absorption losses of 0.01, 0.02, 0.1, 1, and 5 dB/cm are illustrated. A waveguide width and SiO_2 spacer thickness of 600 and 600 nm are selected, respectively.

Figure 4(a) displays the normalized magnetic field in the x-direction $|H_x|/|H_{x,\text{max}}|$ generated by the Au electromagnet at I_{driv} = 120 mA. In Fig. 4(a), $|H_x|_{\text{max}} \approx 80$ Oe, while the spatial average over the garnet layer is approximately 55 Oe. These values agree with the corresponding sheet-current estimate. The garnet therefore operates far below its full-saturation field ($H_{\text{sat}} \approx$ 2000 Oe). However, a phase shift of π can still be obtained between the counter propagating lightwaves via electro-magneto-optical computation. In Fig. 4(b)-(c), the normalized optical mode field distribution in terms of $|H_{\text{op},x}|/|H_{\text{op},x}|_{\text{max}}$ and power $(|E_{\text{op}}|^2/(|E_{\text{op}}|^2)_{\text{max}})$ are depicted, respectively.

Optics EXPRESS

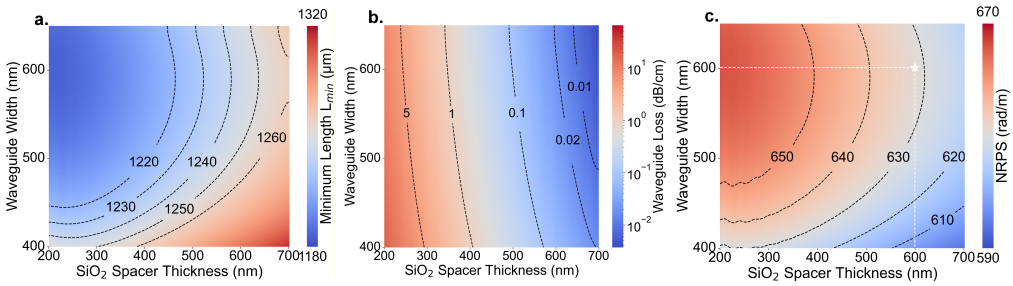


Fig. 3. (a) Monolithic Bi:TbIG/Si waveguide $L_{\min}$ required to induce a π phase shift between the forward and backward propagating lightwave as a function of waveguide width and SiO_2 spacer thickness. (b) Waveguide propagation loss contributed by metal absorption as a function of waveguide width and SiO_2 spacer thickness. (c) Monolithic Bi:TbIG/Si waveguide NRPS as a function of waveguide width and SiO_2 spacer thickness.

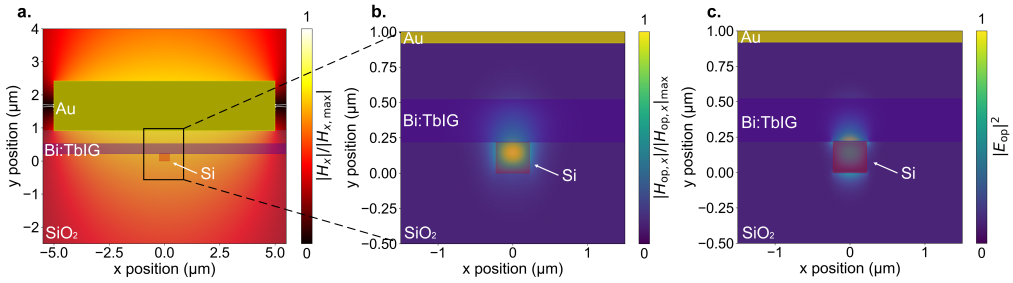


Fig. 4. (a) Normalized magnetic field $|H_x|/|H_{x,\max}|$ from the Au electromagnet in the Bi:TbIG garnet ($|H_x|_{\max} \approx 80$ Oe). Zoomed-in normalized optical mode distributions in the Bi:TbIG/Si waveguide: (b) $|H_{\mathrm{op},x}|/|H_{\mathrm{op},x}|_{\max}$; (c) $|E_{\mathrm{op}}|^2/\left(|E_{\mathrm{op}}|^2\right)_{\max}$.

5. Experimental characterization

During the experimental characterization of the fabricated isolator, a tunable laser (C-band) and photodetector were used at the input and output interfaces, respectively. A 175 nm-wide inverse taper was implemented for low-loss coupling to lensed fibers on both facets. Normalized transmission spectrum of a Si reference waveguide is shown in Fig. 5(a). Four DC probes are used for I_{driv} to generate the necessary H_x for optical isolation. After burn-in, the resistance of an individual electrode strip was measured at $\sim 2\,\Omega$. In Fig. 5(a)-(d), the corresponding forward and backward transmission spectra of a monolithically integrated Bi:TbIG/Si isolator are shown for $I_{\mathrm{driv}} = 0, 41, 79$, and 114 mA. The currents on both arms are equal in amplitude but in opposite directions. This results in approximately 52 mW (26 mW on each side) of standby power consumption for maximum isolation, highlighting the advantage of this device in terms of efficiency [12,20,48,49]. When $I_{\mathrm{driv}} = 0$ mA, the device is reciprocal and therefore there is no wavelength splitting between the forward and backward fringes. The isolator insertion loss is determined to be about -12 dB as compared to a straight reference waveguide. With greater I_{driv} from Fig. 5(a)-(d), splitting between the forward and backward fringes is increased, due to the enhanced nonreciprocal phase difference between the two directions. A π phase difference between the forward and backward propagating lightwave is obtained when $I_{\mathrm{driv}} = 114$ mA (Fig. 5(d)), where an optical isolation ratio of 24 dB is realized. To assess the operational repeatability, forward and backward transmission spectra were recorded after the 10th and 20th current cycles. The isolation response remained consistent over the 20 cycles, showing negligible

Optics EXPRESS

drift in the isolation ratio and fringe splitting, with the electrode resistance unchanged at ~2 Ω. We note that Joule heat generation is equal on two arms and thus does not introduce extra phase shift difference. We also simulated the temperature change when applying a current of 114 mA, as shown in Supplement 1 S4. This conclusion is further supported by the weak temperature dependence of Faraday rotation reported for a related Bi:TbIG film near room temperature [50]. The experimental value of isolator nonreciprocal phase shift at the current level corresponds closely to that obtained via simulations shown in Fig. 4(a), which predicts a value of 120 mA. When I_{driv} is switched off, no remanent isolation is observed, which is attributed to the polycrystalline Bi:TbIG layer relaxing into a low remanence magnetic configuration. As summarized in Table 1, our device demonstrates competitive isolation performance, an isolation-to-insertion-loss ratio of 2.0 dB/dB, comparable to bonded Ce:YIG isolators, while combining monolithic integration, seedlayer-free Bi:TbIG, and on-chip electrical drive in a single platform. Further reduction of the Bi:TbIG propagation loss is expected to improve this ratio and the overall device performance. This demonstration critically highlights the feasibility of magnetooptical isolator platforms with a significantly reduced thermal budget than now.

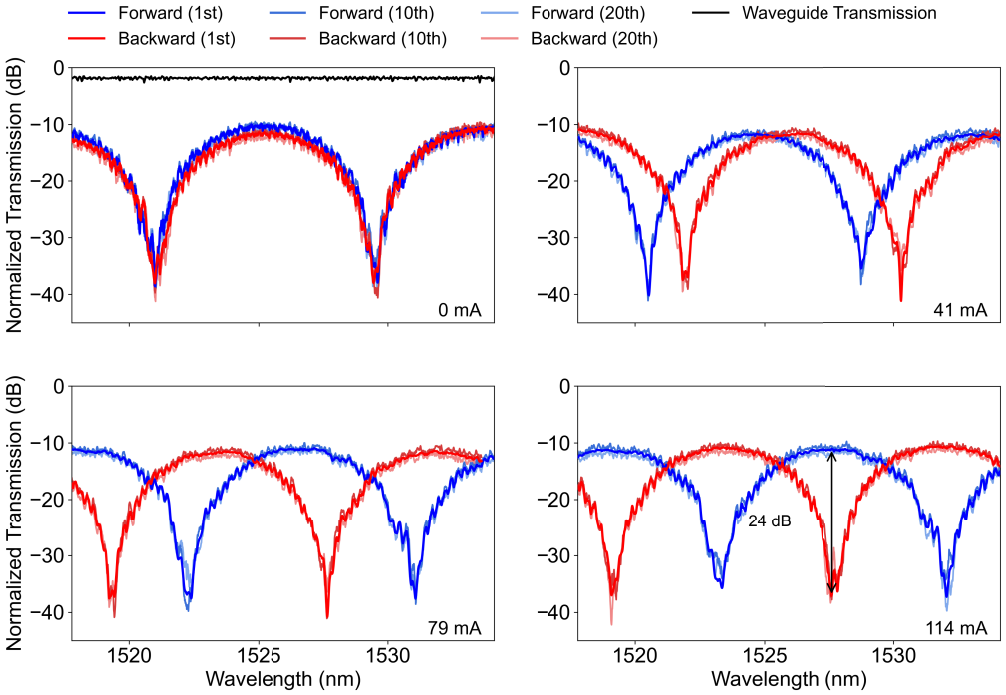


Fig. 5. Measured forward and backward propagating spectra after the 1st, 10th, and 20th on/off cycles when (a) I_{driv} = 0 mA, (b) I_{driv} = 41 mA, (c) I_{driv} = 79 mA, (d) I_{driv} = 114 mA.

6. Conclusion

This work presents the development, and experimental demonstration of a monolithic Si isolator based on a Bi:TbIG seedlayer-free monolithic platform. The elimination of seedlayer allows for enhanced magneto-optical interactions with the waveguide mode and reduced thermal budget. In addition, this approach enables integration of micro-electromagnets in close proximity to the waveguide to reduce driving current and power consumption. To that effect, we demonstrate nonreciprocal phase shift with 114 mA driving current, achieving an optical isolation ratio of

Optics EXPRESS

24 dB with a power consumption of 52 mW. This work sets the stage for the advancement of monolithic seedlayer-free isolators in silicon photonics.

Table 1. Comparison of integrated photonic isolators on silicon.

Reference	Mechanism	Material	Seedlayer	Integration	L_{NRPS} (mm)	Footprint (mm^2)	Isolation (dB)	Isolation/IL (dB/dB)	Power (mW)
Shoji *et al.* (2008) [51]	MO	Ce:YIG	No	Bonding	~0.9	1.5×1.5	21	2.6	0[a]
Bi *et al.* (2011) [33]	MO	Ce:YIG/YIG	Yes	Monolithic	–	0.29×0.29	19.5	1.0	0[a]
Ghosh *et al.* (2012) [21]	MO	Ce:YIG	No	Bonding	–	1.5×0.004	25	3.1	0[a]
Du *et al.* (2018) [52]	MO	Ce:YIG/YIG	Yes	Monolithic	–	–	40	13.3	0[a]
Zhang *et al.* (2019) [34]	MO	Ce:YIG/YIG	Yes	Monolithic	0.968	0.94×0.33	30	6.0	0[a]
Pintus *et al.* (2019) [18]	MO	Ce:YIG	No	Bonding	–	–	30	1.7	3
Liang *et al.* (2023) [53]	MO	Ce:YIG	No	Bonding	0.215	–	29	9.7	76
Fan *et al.* (2012) [54]	Nonlinear	Si	N/A	Monolithic	N/A	0.04×0.04	~20	~1.7	–[b]
Del Bino *et al.* [55]	Nonlinear	Silica	N/A	Monolithic	N/A	–	>24	~4.8	~few[b]
Kittlaus *et al.* (2018) [48]	Brillouin	Si	N/A	Monolithic	N/A	–	>20	>20	90[b]
Kittlaus *et al.* (2021) [56]	Brillouin	Si/AlN	N/A	Monolithic	N/A	–	~16	>26	10[c]
Tzuang *et al.* (2014) [49]	Spatiotemporal	Si (PN)	N/A	Monolithic	N/A	–	–	–	>160[c]
Dostart *et al.* (2021) [57]	Spatiotemporal	Si (PN)	N/A	Monolithic	N/A	–	13	0.7	~0.5[c]
This work	MO	Bi:TbIG	No	Monolithic	1.243	1.5×0.5	24	2.0	52

[a]External permanent magnet.
[b]Optical pump power.
[c]RF electrical drive.

Funding. U.S. National Science Foundation (ECCS-2028199, ECCS-2328839); Ministry of Education (Tier 1 Seed Funding Grant(10786), Tier2 (MOE-T2EP50121-0005)); JSPS KAKENHI (20J12063, 22KJ3113, 24K23945).

Acknowledgment. The authors thank MIT.nano for the use of shared experimental facilities.

Disclosures. The authors declare no conflicts of interest.

Data availability. Data underlying the results presented in this paper are not publicly available at this time but may be obtained from the authors upon reasonable request.

Supplemental document. See Supplement 1 for supporting content.

References

1. J. X. B. Sia, X. Li, J. Wang, *et al.*, "Wafer-scale demonstration of low-loss (~0.43dB/cm), high-bandwidth (>38 ghz), silicon photonics platform operating at the c-band," IEEE Photonics J. **14**(3), 1–9 (2022).
2. A. Rahim, J. Goyvaerts, B. Szelag, *et al.*, "Open-access silicon photonics platforms in europe," IEEE J. Sel. Top. Quantum Electron. **25**(5), 1–18 (2019).
3. S. Y. Siew, B. Li, F. Gao, *et al.*, "Review of silicon photonics technology and platform development," J. Lightwave Technol. **39**(13), 4374–4389 (2021).
4. L. Ranno, J. X. B. Sia, K. P. Dao, *et al.*, "Multi-material heterogeneous integration on a 3-d photonic-cmos platform," Opt. Mater. Express **13**(10), 2711 (2023).
5. J. Feldmann, N. Youngblood, C. D. Wright, *et al.*, "All-optical spiking neurosynaptic networks with self-learning capabilities," Nature **569**(7755), 208–214 (2019).

Optics EXPRESS

6. M. Prabhu, C. Errando-Herranz, L. De Santis, *et al.*, "Individually addressable and spectrally programmable artificial atoms in silicon photonics," Nat. Commun. **14**(1), 2380 (2023).
7. L. Ranno, Y. Z. Tan, C. S. Ong, *et al.*, "Crown ether decorated silicon photonics for safeguarding against lead poisoning," Nat. Commun. **15**(1), 3820 (2024).
8. J. H. Winters, R. D. Gitlin, and S. Kasturia, "Reducing the effects of transmission impairments in digital fiber optic systems," IEEE Commun. Mag. **31**(6), 68–76 (1993).
9. Y. Ibrahimi, S. Boust, Q. Wilmarth, *et al.*, "Low fsr mode-locked laser based on inp-si$_3$n$_4$ hybrid integration," J. Lightwave Technol. **39**(24), 7573–7580 (2021).
10. M. E. Storm, "Controlled retroreflection: a technique for understanding and eliminating parasitic lasing," J. Opt. Soc. Am. B **9**(8), 1299 (1992).
11. B. Haq, S. Kumari, K. Van Gasse, *et al.*, "Micro-transfer-printed iii-v-on-silicon c-band semiconductor optical amplifiers," Laser Photonics Rev. **14**(7), 1900364 (2020).
12. H. Tian, J. Liu, A. Siddharth, *et al.*, "Magnetic-free silicon nitride integrated optical isolator," Nat. Photonics **15**(11), 828–836 (2021).
13. Q. Lin, J. Wang, and S. Fan, "Compact dynamic optical isolator based on tandem phase modulators," Opt. Lett. **44**(9), 2240 (2019).
14. A. D. White, G. H. Ahn, K. Van Gasse, *et al.*, "Integrated passive nonlinear optical isolators," Nat. Photonics **17**(2), 143–149 (2023).
15. K. Wang, S. Gao, Y. Wang, *et al.*, "Four-wave-mixing based silicon integrated optical isolator with dynamic non-reciprocity," in *2017 Conference on Lasers and Electro-Optics Pacific Rim (CLEO-PR)*, (2017), pp. 1–2.
16. C. G. Poulton, R. Pant, A. Byrnes, *et al.*, "Design for broadband on-chip isolator using stimulated brillouin scattering in dispersion-engineered chalcogenide waveguides," Opt. Express **20**(19), 21235 (2012).
17. M. Yu, R. Cheng, C. Reimer, *et al.*, "Integrated electro-optic isolator on thin-film lithium niobate," Nat. Photonics **17**(8), 666–671 (2023).
18. P. Pintus, D. Huang, P. A. Morton, *et al.*, "Broadband te optical isolators and circulators in silicon photonics through ce:yig bonding," J. Lightwave Technol. **37**(5), 1463–1473 (2019).
19. D. Minemura, R. Kou, Y. Sutoh, *et al.*, "Compact magneto-optical isolator by u-transfer printing of magneto-optical single-crystal film on silicon waveguides," Opt. Express **31**(17), 27821–27829 (2023).
20. D. Huang, P. Pintus, Y. Shoji, *et al.*, "Silicon-based integrated polarization-independent magneto-optical isolator," Opt. Lett. **42**(23), 4901 (2017).
21. S. Ghosh, S. Keyvavinia, W. Van Roy, *et al.*, "Ce:yig/silicon-on-insulator waveguide optical isolator realized by adhesive bonding," Opt. Express **20**(2), 1839 (2012).
22. P.-H. Liu, B. K. Moghal, and B. J. H. Stadler, "Effect of composition and two-step annealing on Ce-doped terbium iron garnets on Si," Opt. Mater. Express **15**(7), 1407–1418 (2025).
23. W. Yan, Z. Wei, Y. Yang, *et al.*, "Ultra-broadband magneto-optical isolators and circulators on a silicon nitride photonics platform," Optica **11**(3), 376 (2024).
24. K. Srinivasan and B. J. H. Stadler, "Review of integrated magneto-optical isolators with rare-earth iron garnets for polarization diverse and magnet-free isolation in silicon photonics [invited]," Opt. Mater. Express **12**(2), 697 (2022).
25. C. Zhang, P. Dulal, B. J. H. Stadler, *et al.*, "Monolithically-integrated te-mode 1d silicon-on-insulator isolators using seedlayer-free garnet," Sci. Rep. **7**(1), 5820 (2017).
26. M. Guillot, H. Le Gall, J. M. Desvignes, *et al.*, "Low-temperature anisotropy of the faraday rotation in the samarium iron garnet," IEEE Trans. Magn. **30**(6), 4419–4421 (1994).
27. P. Dulal, A. D. Block, T. E. Gage, *et al.*, "Optimized magneto-optical isolator designs inspired by seedlayer-free terbium iron garnets with opposite chirality," ACS Photonics **3**(10), 1818–1825 (2016).
28. T. Fakhrul, S. Tazlaru, B. Khurana, *et al.*, "High figure of merit magneto-optical ce- and bi-substituted terbium iron garnet films integrated on si," Adv. Opt. Mater. **9**(16), 2100512 (2021).
29. Y. Shi, Z. Yu, and S. Fan, "Limitations of nonlinear optical isolators due to dynamic reciprocity," Nat. Photonics **9**(6), 388–392 (2015).
30. A. Pitilakis, D. Chatzidimitriou, T. V. Yioultsis, *et al.*, "Asymmetric si-slot coupler with nonreciprocal response based on graphene saturable absorption," IEEE J. Quantum Electron. **57**(3), 1–10 (2021).
31. D. Chatzidimitriou, A. Pitilakis, T. Yioultsis, *et al.*, "Breaking reciprocity in a non-hermitian photonic coupler with saturable absorption," Phys. Rev. A **103**(5), 053503 (2021).
32. D. B. Sohn, O. E. Örsel, and G. Bahl, "Electrically driven optical isolation through phonon-mediated photonic autler–townes splitting," Nat. Photonics **15**(11), 822–827 (2021).
33. L. Bi, J. Hu, P. Jiang, *et al.*, "On-chip optical isolation in monolithically integrated non-reciprocal optical resonators," Nat. Photonics **5**(12), 758–762 (2011).
34. Y. Zhang, Q. Du, C. Wang, *et al.*, "Monolithic integration of broadband optical isolators for polarization-diverse silicon photonics," Optica **6**(4), 473 (2019).
35. X. Sun, Q. Du, T. Goto, *et al.*, "Single-step deposition of cerium-substituted yttrium iron garnet for monolithic on-chip optical isolation," ACS Photonics **2**(7), 856–863 (2015).
36. A. D. Block, P. Dulal, B. J. H. Stadler, *et al.*, "Growth parameters of fully crystallized yig, bi:yig, and ce:yig films with high faraday rotations," IEEE Photonics J. **6**(1), 1–8 (2014).

Optics EXPRESS

37. K. Srinivasan, C. Zhang, P. Dulal, *et al.*, "High-gyrotropy seedlayer-free ce:tbig for monolithic laser-matched soi optical isolators," ACS Photonics **6**(10), 2455–2461 (2019).
38. D. Dai and J. E. Bowers, "Novel concept for ultracompact polarization splitter-rotator based on silicon nanowires," Opt. Express **19**(11), 10940–10949 (2011).
39. N. N. Feng, R. Sun, J. Michel, *et al.*, "Low-loss compact-size slotted waveguide polarization rotator and transformer," Opt. Lett. **32**(15), 2131–2133 (2007).
40. K. Hayashi, K. P. Dao, M. J. Gross, *et al.*, "Magneto-optical bi-substituted yttrium and terbium iron garnets for on-chip crystallization via microheaters," Adv. Opt. Mater. **12**(25), 2400708 (2024).
41. J. Wang, T. Zhang, Y. Yang, *et al.*, "Crystallization kinetics and perpendicular anisotropy of yig thin films grown on sio2/si substrates using localized laser annealing," Adv. Funct. Mater. **36**(37), e27741 (2026).
42. B. J. H. Stadler and T. Mizumoto, "Integrated magneto-optical materials and isolators: A review," IEEE Photonics J. **6**(1), 1–15 (2014).
43. M. C. Onbasli, L. Beran, M. Zahradník, *et al.*, "Optical and magneto-optical behavior of cerium yttrium iron garnet thin films at wavelengths of 200–1770 nm," Sci. Rep. **6**(1), 23640 (2016).
44. F. P. Payne and J. P. R. Lacey, "A theoretical analysis of scattering loss from planar optical waveguides," Opt. Quantum Electron. **26**(10), 977–986 (1994).
45. R. Ma, S. Reniers, Y. Shoji, *et al.*, "Integrated polarization-independent optical isolators and circulators on an inp membrane on silicon platform," Optica **8**(12), 1654–1661 (2021).
46. Y. Shoji and T. Mizumoto, "Silicon waveguide optical isolator with directly bonded magneto-optical garnet," Appl. Sci. **9**(3), 609 (2019).
47. K. Sato, M. Okano, and Y. Shoji, "Ultra-compact microring optical isolator using an aluminum-substituted cobalt ferrite thin film," Optica **11**(6), 889–895 (2024).
48. E. A. Kittlaus, N. T. Otterstrom, P. Kharel, *et al.*, "Non-reciprocal interband brillouin modulation," Nat. Photonics **12**(10), 613–619 (2018).
49. L. D. Tzuang, K. Fang, P. Nussenzveig, *et al.*, "Non-reciprocal phase shift induced by an effective magnetic flux for light," Nat. Photonics **8**(9), 701–705 (2014).
50. H. Li, D. Zhang, Y. Zhang, *et al.*, "Giant reduced magnetic anisotropy in magneto-optical garnet," Results Phys. **60**, 107625 (2024).
51. Y. Shoji, T. Mizumoto, H. Yokoi, *et al.*, "Magneto-optical isolator with silicon waveguides fabricated by direct bonding," Appl. Phys. Lett. **92**(7), 071117 (2008).
52. Q. Du, T. Fakhrul, Y. Zhang, *et al.*, "Monolithic magneto-optical oxide thin films for on-chip optical isolation," MRS Bull. **43**(6), 413–418 (2018).
53. J. Liang, Y. Li, T. Dai, *et al.*, "On-chip Ce:YIG/Si Mach–Zehnder optical isolator with low power consumption," Opt. Express **31**(5), 8375–8383 (2023).
54. L. Fan, J. Wang, L. T. Varghese, *et al.*, "An all-silicon passive optical diode," Science **335**(6067), 447–450 (2012).
55. L. Del Bino, J. M. Silver, M. T. M. Woodley, *et al.*, "Microresonator isolators and circulators based on the intrinsic nonreciprocity of the Kerr effect," Optica **5**(3), 279–282 (2018).
56. E. A. Kittlaus, W. M. Jones, P. T. Rakich, *et al.*, "Electrically driven acousto-optics and broadband non-reciprocity in silicon photonics," Nat. Photonics **15**(1), 43–52 (2021).
57. N. Dostart, H. Gevorgyan, D. Onural, *et al.*, "Optical isolation using microring modulators," Opt. Lett. **46**(3), 460 (2021).